ROYAL SOCIETY
OF CHEMISTRY

EDGE ARTICLE

Check for updates

All publication charges for this article
have been paid for by the Royal Society
of Chemistry

All-in-one mitochondria-targeted NIR-II fluorophores for cancer therapy and imaging†

Yujia Zheng,‡[ab] Qianqian Li,‡[ab] Jing Wu,[a] Ziyi Luo,[a] Wenyi Zhou,[a] Anguo Li,[a] Yanling Chen,[a] Tuerxunayi Rouzi,[a] Tian Tian,[b] Hui Zhou, [ID] [ad] Xiaodong Zeng, [ID] [ad] Yang Li,[ad] Xiaoding Cheng,[ad] Yongchang Wei,[c] Zixin Deng,[a] Fuling Zhou*[a] and Xuechuan Hong [ID] *[abd]

Small-molecule subcellular organelle-targeting theranostic probes are crucial for early disease diagnosis and treatment. The imaging window of these molecules is mainly focused on the visible and near-infrared region (below ∼900 nm) which limits the tissue penetration depth and therapeutic effects. Herein, a novel NIR-II small-molecule probe **H4−PEG-Glu** with a thiopyrylium cation was synthesized. **H4−PEG-Glu** not only can quickly and effectively image mitochondria in acute myeloid leukemia (AML) cells, and induce G_0/G_1 phase arrest by the intrinsic mitochondrial apoptosis pathway w/o irradiation, but also exhibit moderate cytotoxicity against AML cancer cells in a dose dependent-manner without laser irradiation. The THP-1 cells treated with **H4−PEG-Glu** upon NIR laser irradiation showed enhanced chemo- and photothermal therapy (CPTT) with 93.07% ± 6.43 apoptosis by Annexin V staining. Meanwhile, **H4−PEG-Glu** displayed high synergistic CPTT effects *in vivo*, as well as specific NIR-II tumor imaging in AML patient derived PDX mouse models for the first time. Our work lays down a solid foundation for designing small-molecule NIR-II mitochondria-selective theranostic probes.

Introduction

Mitochondria, as an important type of subcellular organelles, plays an essential role in energy production and cell survival.[1] Mitochondria regulates many cellular behaviors such as cellular signaling, differentiation, growth, apoptosis, metabolism and death.[2] Because of the importance of mitochondria in cellular regulation and death, a number of small-molecule mitochondria-targeted theranostic probes, including rhodamine, triphenyl phosphonium (TPP), F16, dequalinium (DQA), and guanidine have been developed.[3] Furthermore, when introducing 2-deoxy-D-glucose into theranostic probes, it is possible to enhance their potency against drug-resistant tumors in one delivery system.[4] It is worth noting that an F16 derivative **5BMF** was firstly accomplished with an IC_{50} value of ∼50 nM against H2228 cells and *in vivo* fluorescence imaging at

∼550 nm.[5] However, small-molecule subcellular organelle-targeting theranostic probes are still in their infancy. The imaging window of these molecules is mainly focused on the visible and near-infrared region (below ∼900 nm) which still limits the tissue penetration depth and therapeutic effects. Acute Myeloid Leukemia (AML) is a heterogeneous and complex hematological malignancy that affects ∼1 million people each year globally.[6] Various treatments such as molecularly targeted chemotherapy and allogeneic hematopoietic stem cell transplantation (HSCT) have been extensively applied in clinic treatment.[7] However, the 5 year survival rate for patients 20 years older with AML is still quite gloomy (∼25%), and the treatment of AML remains one of the most formidable challenges in clinic research. Recent developments in cancer therapy were mostly focused on solid tumor models, and very few small-molecule probes have been exploited for the diagnosis and treatment of AML owing to the circulation of cancer cells in the immune system.[8] Thus, it is imperative to pursue a novel therapeutic strategy for AML.

In recent years, fluorescence imaging in the second near-infrared window (NIR-II, 1000–1700 nm) has emerged as a novel technique, and been widely used in tumor imaging, image-guided surgery and therapy with deep tissue penetration and subcellular resolution.[9] To date, several types of NIR-II inorganic materials,[10] macromolecules[11] and small-molecule fluorophores,[12] such as quantum dots,[13] ultrafine gold nanoclusters,[14] single-walled carbon nanotubes,[15] rare earth

[a]*Department of Hematology, Zhongnan Hospital of Wuhan University, State Key Laboratory of Virology, Wuhan University School of Pharmaceutical Sciences, Wuhan 430071, China. E-mail: Xhy78@whu.edu.cn; zhoufuling@whu.edu.cn*

[b]*College of Science, Innovation Center for Traditional Tibetan Medicine Modernization and Quality Control, Tibet University, Lhasa, 850000, China*

[c]*Department of Radiation Oncology, Zhongnan Hospital of Wuhan University, Wuhan, 430071, China*

[d]*Shenzhen Institute of Wuhan University, Shenzhen 518057, China*

† Electronic supplementary information (ESI) available. See DOI: 10.1039/d0sc04727a

‡ These authors contributed equally to this work.

nanoparticles,[16] and **CH1055**,[17] have been reported. Of note, organic dyes **FD-1080**,[18] **HQL2**,[19] **HL3** (ref. 20) and **2TT-oC26B**[21] were employed for NIR-IIb (1500–1700 nm) lymphatic drainage, the whole body, cerebral vasculature and vascular imaging with unparalleled tissue-imaging depths, near-zero auto-fluorescence and negligible scattering. Among them, a few of the inorganic fluorophores had potential safety concerns in clinic translation because of high uptakes and long-term retention in the immune system.[22] Currently, small-molecule NIR-II fluorophores are mainly focused on donor–acceptor–donor (D–A–D) or polymethine structures.[23] However, no research based on small-molecule mitochondria-targeted NIR-II imaging technology has been reported for *in vivo* AML imaging, and anti-AML chemo- and photothermal therapy.[24] Herein, NIR-II thiopyrylium fluorophores **H4–PEG2K** and **H4–PEG-Glu** were synthesized based on our previous reports.[25] Then, anti-cancer cell activity, the selective mitochondria-targeting ability and photothermal properties of NIR-II probes **H4–PEG2K** and **H4–PEG-Glu** against THP-1 and Molm-13 cells were investigated. *In vitro* cell studies of **H4–PEG-Glu** showed high affinity and moderate cytotoxicity against THP-1 and Molm-13 cells. Upon 808 nm laser irradiation, **H4–PEG-Glu** produced hyperthermia and showed enhanced cellular cytotoxicity toward AML cells, exhibiting synergistic CPTT effects. An enhanced cytotoxicity with 93.07% ± 6.43 and 89.44% ± 2.84 apoptosis of THP-1 and Molm-13 cells was observed by Annexin V staining through flow cytometry. It was further demonstrated that **H4–PEG-Glu** induced G_0/G_1 phase arrest w/o irradiation and showed super mitochondria-targeted bioimaging in live cancer cells. Subsequently, AML patient derived PDX mouse models were, for the first time, adopted for NIR-II imaging and image-guided CPPT. In addition, a high level of accumulation was also observed in the bone marrow of the AML models. The leukemia stem cell (LSC) population CD34^{+} decreased sharply under irradiation in comparison to the other groups, manifesting high synergistic CPTT effects of **H4–PEG-Glu** toward AML *in vivo*. In a proof-of-concept study, we have developed a small-molecule NIR-II mitochondria-selective theranostic agent for the real-time imaging and therapy of AML in AML patient derived PDX mouse models, which could be a powerful biomedical research tool for detection, imaging and image-guided therapy of AML with a good safety profile, subcellular resolution and deep tissue penetration.

Results and discussion

Lipophilic or delocalized cations (LDC) play a crucial role in designing mitochondria-specific delivery of imaging and therapeutic agents. LDC can distribute electrophoretically into the mitochondrial matrix in response to the electric potential between the inner and the outer mitochondrial membrane. Therefore, simple molecular cations with synergetic mitochondria targeted chemo- and photothermal therapy may be capable of exerting all-in-one theranostic anti-tumor activity against AML. Thus, we utilized a thiopyrylium cation as an NIR acceptor to construct a novel mitochondria-targeted NIR-II chemo- and photothermal therapeutic dye **H4–PEG-Glu**. First,

we designed and synthesized an unsymmetrical fluorophore **H4** through a condensation reaction between the key intermediate thiopyrylium tetrafluoroborate **1** and aldehyde **2** in acetic anhydride at 75 °C for 2 h under microwave irradiation in 52% yield (see ESI†).[25] To further explore the biological application, **H4** was further conjugated with **PEG-Glu** *via* a Cu-catalyzed click reaction to afford **H4–PEG-Glu** in anhydrous DMF in 52.5% yield (Fig. 1e). The highest occupied molecular orbital (HOMO, −5.30 eV) and the lowest unoccupied molecular orbital (LUMO, −3.60 eV) of **H4–PEG-Glu** were obtained by DFT calculations with the B3LYP exchange functional employing 6-31G(d) basis sets (Fig. 1f). The E_{gap} (1.7 eV) of **H4–PEG-Glu** was close to that of **CH1055** (1.5 eV) with a typical NIR-II optical E_{gap} based on previous results.[17] **H4–PEG-Glu** was further purified using HPLC
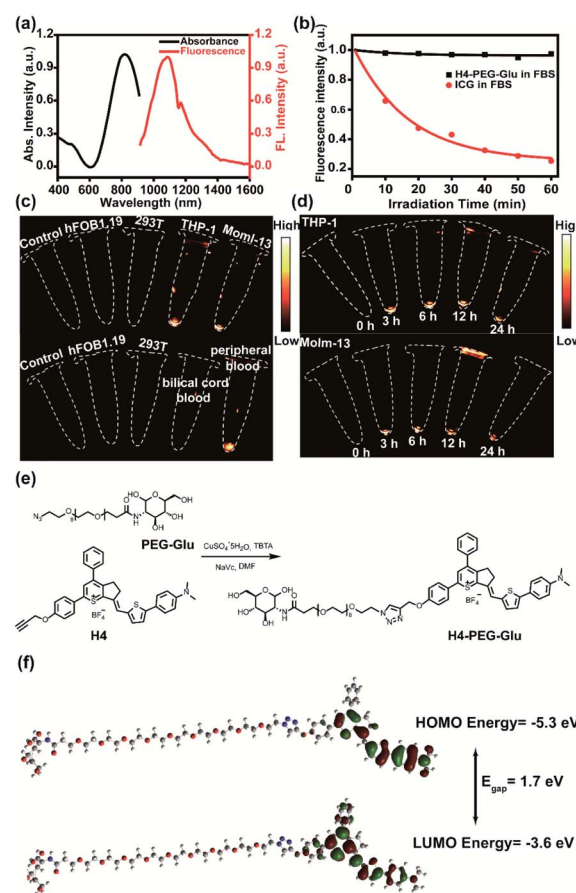

Fig. 1 (a) UV absorbance of **H4−PEG-Glu** (black line) and NIR-II fluorescence emission of **H4−PEG-Glu** (red line) with a peak at ~1085 nm and a shoulder peak at ~1200 nm under an 808 nm excitation laser (solvents: dichloromethane). (b) The photostability of **H4−PEG-Glu** and ICG in FBS under continuous 808 nm laser (180 mW cm^{-2}, 50 ms) irradiation for 60 min. (c) NIR-II images of different cells including 293T, THP-1, hFOB1.19, THP-1, Molm-13, peripheral blood donated from AML patients and umbilical cord blood by **H4−PEG-Glu** under 808 nm excitation (1000 LP and 20 ms). (d) NIR-II images of THP-1 and Molm-13 cells by **H4−PEG-Glu** with different incubation times. (e) The synthetic route to **H4−PEG-Glu**; (f) HOMO and LUMO orbital surfaces of **H4−PEG-Glu** using DFT B3LYP/6-31G(d) scrf = (cpcm, solvent = dichloromethane) method. $E_{gap} = E_{LUMO} − E_{HOMO}$.

and all compounds were characterized by ^{1}H-NMR, ^{13}C-NMR, HRMS and MALDI-TOF-MS (Fig. S1–S6†).

H4–PEG-Glu exhibited excellent solubility in common organic solvents and high aqueous solubility. The UV-vis-NIR absorption and NIR-II fluorescence emission spectra of **H4–PEG-Glu** in CH_2Cl_2 were investigated under 808 nm excitation. As shown in Fig. 1a, the absorption peak was at ~810 nm, while the fluorescence emission peak was at ~1085 nm and a shoulder peak was at ~1200 nm. The NIR-II quantum yield (QY) of **H4–PEG-Glu** in fetal bovine serum (FBS) was measured to be ~1.3% under 808 nm laser excitation using IR-26 dye as a reference (QY = 0.5%) (Fig. S7†). **H4–PEG-Glu** showed spherical shapes with an average particle size of ~96 nm and hydrodynamic radius of ~120 nm, as determined from transmission electron microscopy (TEM) and dynamic light scattering (DLS), respectively (Fig. S8†). **H4–PEG-Glu** displayed negligible decay in FBS under continuous 808 nm laser irradiation at a power density of 180 mW cm^{-2} for 60 min (50 ms exposure time), while indocyanine green (ICG) exhibited a sharp decrease in fluorescence intensity under the same conditions, indicating its high resistance to photo-bleaching for NIR-II biomedical application (Fig. 1b). Additionally, the cellular uptake behavior and imaging ability of ALM cancer cells were also investigated. As depicted in Fig. 1c and d, the human myeloid leukemia mononuclear cells THP-1 and Molm-13 exhibited high affinity and strong intracellular NIR-II fluorescence whereas negligible binding was observed in 293T and hFOB1.19 cells treated with **H4–PEG-Glu** (20 μM) (Fig. 1c). The THP-1 and Molm-13 cell lines can be clearly visualized after 3 h of incubation, and fluorescence signals reach a maximum at 6 h, while **H4–PEG2K** has demonstrated almost no targeting ability without the glucose moiety (Fig. 1d, Fig. S12a and b†). To further illustrate the specificity toward AML cancer cells, we further studied the cellular uptake behavior in peripheral blood donated from AML patients and umbilical cord blood collected from healthy people (Fig. 1c). We were delighted to find out that the peripheral blood samples had bright NIR-II fluorescence instead of umbilical cord blood, indicating that **H4–PEG-Glu** has an AML targeting and accumulation capability and is a promising candidate for targeted NIR-II imaging.

The cell viabilities of **H4–PEG-Glu** were investigated by CCK-8 assays with 293T, hFOB1.19, THP-1 and Molm-13 cell lines with different concentrations within 24 h without laser irradiation. As shown in Fig. 2a, no obvious cytotoxicity of **H4–PEG-Glu** was observed even at higher concentrations up to 60 μM, suggesting **H4–PEG-Glu** had excellent biocompatibility toward 293T and hFOB1.19 normal cells (Fig. 2a). In contrast, **H4–PEG-Glu** suppressed proliferation of AML cells (THP-1 and Molm-13) in a concentration-dependent manner with IC$_{50}$ values of 23.97 ± 3.24 and 29.66 ± 1.09 μM, respectively, indicating a specific cytotoxic effect against AML cells without laser irradiation (Fig. 2a). Thereafter, we evaluated the photothermal performance of **H4–PEG-Glu**. The temperature of **H4–PEG-Glu** in serum at various concentrations (0 μM, 10 μM, 20 μM, 40 μM, 60 μM, 80 μM) was recorded under 808 nm laser irradiation at a power density of 1.2 W cm^{-2} for 5 min. Rapid photothermal effects occurred on laser irradiation even at the dose of 40 μM
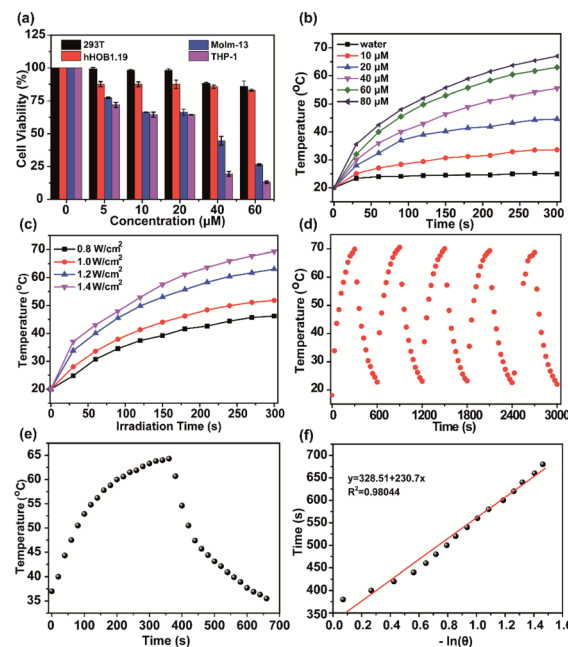

Fig. 2 (a) The cell viability of 293T, THP-1, hFOB1.19, and Molm-13 after incubation with different concentrations of **H4–PEG-Glu** for 24 h without laser irradiation ($n = 6$). (b) Temperature variation of **H4–PEG-Glu** in serum at various concentrations under irradiation by an 808 nm laser at a power density of 1.2 W cm^{-2} for 5 min. (c) Temperature variation of **H4–PEG-Glu** in serum (60 μM) under 808 nm laser irradiation at different power densities. (d) Temperature elevation of **H4–PEG-Glu** (60 μM) in serum over several ON/OFF cycles involving irradiation with an 808 nm laser (1.4 W cm^{-2}) for 5 min followed by passive cooling. (e) Photothermal conversion ability of **H4–PEG-Glu** (60 μM) under 808 nm laser irradiation (1.2 W cm^{-2}) for 5.5 min and naturally cooled to ambient temperature. (f) Liner time data versus $-\ln(\theta)$ during the cooling period.

(Fig. 2b). The temperature increased significantly (up to 63 °C) at the dose of 60 μM by varying the laser power density (1.2 and 1.4 W cm^{-2}) (Fig. 2c). The photothermal stability of **H4–PEG-Glu** (60 μM) in serum was further assessed by continuously monitoring the temperature variation under 808 nm laser irradiation (1.4 W cm^{-2}) for 5 min, and it was naturally cooled to room temperature for five heating/cooling cycles. As shown in Fig. 2d, no obvious decline of temperature was observed in its photothermal conversion performance. The photothermal conversion efficiency of **H4–PEG-Glu** was ~11.6% according to the reported methods (Fig. 2e and f).[26] No significant amount of ROS in vitro was observed in any group of **H4–PEG-Glu** under 808 nm laser irradiation (Fig. S9†). As a consequence, the good photostability and excellent photothermal performance of **H4–PEG-Glu** make it an ideal NIR-II probe for in vivo fluorescence image-guided photothermal therapy.

Subsequently, the photothermal ablation of THP-1 and Molm-13 cells induced by **H4–PEG-Glu** was conducted under 808 nm NIR laser irradiation (1.2 W cm^{-2}). After NIR laser treatment, the cells were observed with a bright-field microscope. As shown in Fig. 3a, **H4–PEG-Glu** (20 μM) treated THP-1 or Molm-13 cells had an enhanced chemo- and photothermal cytotoxicity under NIR irradiation compared to that under PBS,
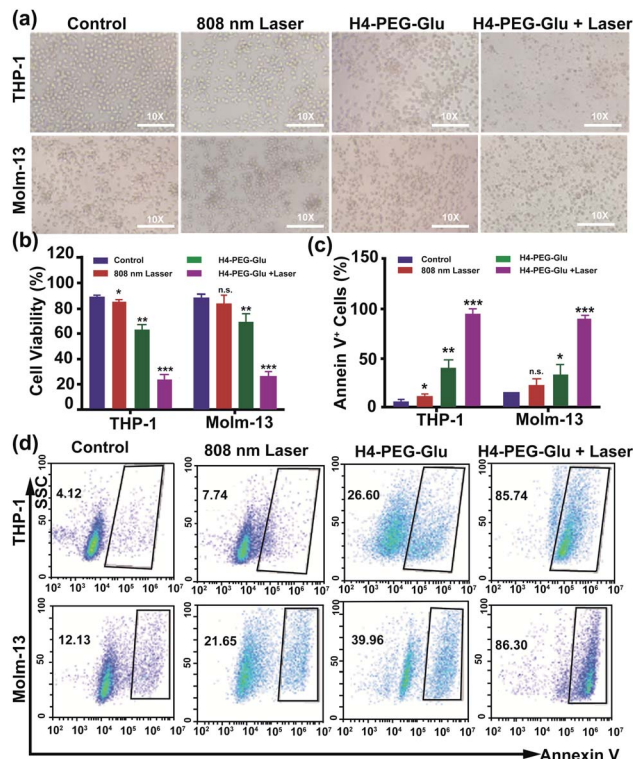
Fig. 3 (a) The bright-field microscopy images of THP-1 and Molm-13 cells treated with PBS, 808 nm laser, H4−PEG-Glu (20 μM), and H4−PEG-Glu (20 μM) under 808 nm laser irradiation (1.2 W cm^{-2}, 5 min). (b) The cell viability of THP-1 and Molm-13 by the Trypan Blue Exclusion test according to the bright-field microscopy images. (c) Proportions of Annexin V+ THP-1 cells and Annexin V+ Molm-13 cells calculated from the cell apoptosis in Fig. 3d. (d) Flow cytometry analysis of cell apoptosis of THP-1 and Molm-13 cells treated with PBS, 808 nm laser, H4−PEG-Glu (20 μM), and H4−PEG-Glu (20 μM) under 808 nm laser irradiation (1.2 W cm^{-2}, 5 min). *$p < 0.05$; **$p < 0.01$; ***$p < 0.001$; ns, not significant.
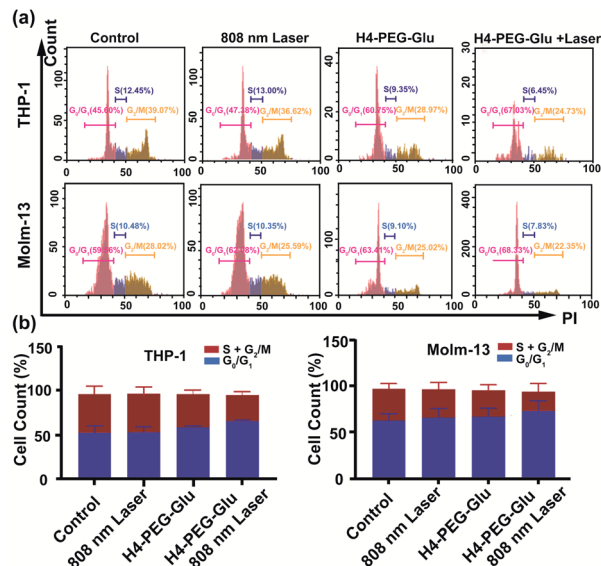

Fig. 4 (a) Flow cytometry analysis of the cell cycle of THP-1 and Molm-13 cells treated with PBS, H4−PEG-Glu (20 μM), and H4−PEG-Glu (20 μM) under 808 nm laser irradiation (1.2 W cm^{-2}, 5 min). (b) Proportions of G_0/G_1, S, and G_2/M phase cells in THP-1 and Molm-13. *$p < 0.05$; **$p < 0.01$; ***$p < 0.001$; ns, not significant.

808 nm laser or H4−PEG-Glu (20 μM) alone. The cell viability of THP-1 and Molm-13 cells was also quantitatively analyzed by the Trypan Blue dye exclusion test. As shown in Fig. 3b, approximately 39.57% ± 5.87 of THP-1 cells and 42.9% ± 5.58 of Molm-13 cells were reduced by H4−PEG-Glu (20 μM) induced synergistic therapy. The apoptosis of THP-1 and Molm-13 cells was also studied by Annexin V staining through flow cytometry. THP-1 and Molm-13 cells treated with H4−PEG-Glu under 808 nm laser irradiation showed an enhanced cytotoxicity with 93.07% ± 6.43 and 89.44% ± 2.84 apoptosis, respectively. The results were in good agreement with the aforementioned cell viability (Fig. 3c and d). All these results demonstrated that the NIR-II probe H4−PEG-Glu exhibited effective chemo- and photothermal synergistic treatment (CPTT) toward ALM cancer cells (THP-1 and Molm-13) *in vitro*.

To further explore the mechanism of toxicity and apoptosis of H4−PEG-Glu, the cell cycle progression of the above cancer cells was analyzed by fluorescence-activated cell sorting (FACS) analysis. THP-1 or Molm-13 cells in the G_0/G_1 phase and G_2/M phase have unreplicated diploid (2n) DNA content and replicated ploid (4n) DNA, implying the different procedures of DNA

replication. As shown in Fig. 4a and b, THP-1 cells treated with H4−PEG-Glu under 808 nm laser irradiation exhibited an obviously increased percentage in the G_0/G_1 phase (53.64% ± 7.46 to 66.68% ± 0.78) and a decreased percentage in the S phase and G_2/M phase (42.24% ± 9.40 to 28.61% ± 3.55), demonstrating that H4−PEG-Glu inhibited DNA replication due to inducing cell cycle arrest in the G_0/G_1 phase. A similar apoptosis pathway was also observed in Molm-13 cells.

Mitochondria is critically important in energy production and apoptosis.[27] To further assess the targeting ability of H4−PEG-Glu to mitochondria and its efficiency in mitochondria-targeted cancer therapy, THP-1 and Molm-13 cells were incubated with H4−PEG-Glu (20 μM) for 24 h followed by staining with Mito-tracker Green (5 μM), a commercial available kit used to label the mitochondria. The intrinsic fluorescence of H4−PEG-Glu (red color) was observed to be completely overlapped with Mito-tracker (Green) (Fig. 5a, Fig. S10†), implying its excellent targeting ability to mitochondria. The feedback of mitochondrial membrane potential (MMP) reflected different cellular status and has been used for assessing the therapeutic effects.[28] Thus, MMP levels of THP-1 and Molm-13 cells in each group were detected using a commercial fluorescent probe JC-1. The fluorescence images of each group have been shown in Fig. 5b. According to Fig. 5b, the red fluorescence signal from THP-1 cancer cells was bright while the green fluorescence signal was weak before H4−PEG-Glu or laser treatment, demonstrating that the MMP level was normal. With the progress of the treatment process, the green fluorescence signal intensified and red fluorescence signal gradually vanished, illustrating the decrease of the MMP level, and the transformation of JC-1 from J-aggregates into monomers. Upon
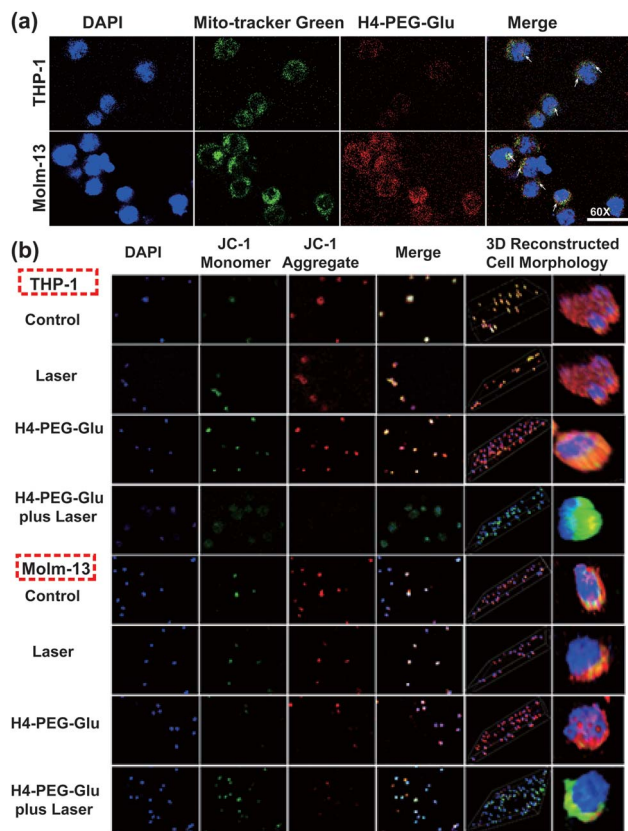
Fig. 5 (a) Confocal fluorescence images of THP-1 and Molm-13 cells treated with **H4–PEG-Glu** (20 μM) for 24 h without laser irradiation. The cell mitochondria stained with Mito-Tracker Green showed a green fluorescence signal, 4′,6-diamidino-2-phenylindole (DAPI) labeled nucleus showed a blue fluorescence signal and **H4–PEG-Glu** showed a red fluorescence signal. (b) Immunofluorescence mitochondrial membrane potential staining images of AML cells with different treatments. The cell nucleus stained with DAPI showed a blue fluorescence signal, JC-1 monomers showed a green fluorescence signal, and JC-1 aggregates showed a red fluorescence signal. *$p <$ 0.05; **$p < 0.01$; ***$p < 0.001$; ns, not significant.

Fig. 6 (a) The representative NIR-II *in vivo* images of AML patient derived PDX mouse models ($n = 3$), the blue arrow points to the location of tumor sites in bone marrow. (b) The schematic diagram of AML patient derived PDX mouse models and treatment. (c) The proportion of CD34$^+$ cells in peripheral blood mononuclear cells (PBMC) and bone marrow (BM) after treatment. (d) The immunohistochemical staining images of bone marrow (up left to right: AML mice without treatment, mice treated with **H4–PEG-Glu**, and mice treated with **H4–PEG-Glu** under 808 nm laser irradiation, down left to right: immunohistochemical staining images were the enlargement of the red square in left images). *$p < 0.05$; **$p < 0.01$; ***$p < 0.001$; ns, not significant.

treatment with **H4–PEG-Glu** under 808 nm laser irradiation, the red fluorescence signals of THP-1 cells vanished, suggesting that the therapeutic effects of THP-1 cancer cells were greatly enhanced. The same phenomenon was also detected in Molm-13 cancer cells. All these results demonstrated that **H4–PEG-Glu** is a novel therapeutic probe with NIR-II fluorescence and mitochondrial-targeting properties.

Inspired by the intriguing chemo- and photothermal performance of **H4–PEG-Glu** *in vitro*, subsequently, we envisioned that **H4–PEG-Glu** can achieve great NIR-II image-guided therapeutic effects *in vivo*. Thus, the NIR-II fluorescence imaging performance of **H4–PEG-Glu** was firstly evaluated *in vivo* using AML patient derived PDX mouse models. **H4–PEG-Glu** (200 μL, 1 μg μL^{-1} in PBS) was first administered into AML patient derived PDX mouse models ($n = 3$) through the tail vein. As shown in Fig. 6a, the fluorescence signal was gradually enhanced at the bone marrow (blue arrow in Fig. 6a) of AML patient derived PDX mouse models, and reached a maximum at

6 h post injection (808 nm excitation, 90 mW cm^{-2}, 1000 LP and 100 ms). In contrast, no obvious signals were detected in bone marrow at all-time points i.v. post-injection of **H4–PEG2K** in the AML patient derived PDX mouse models or in the normal B-NDG mice ($n = 3$), demonstrating that **H4–PEG-Glu** exhibited specific targeting ability to AML cancer cells in bone marrow (Fig. S12c†). Thereafter, AML patient derived PDX mouse models ($n = 4$ group, ~20 g each) were treated with PBS, **H4–PEG-Glu** (200 μg), and **H4–PEG-Glu** (200 μg) under 808 nm laser irradiation (1.2 W cm^{-2}, 5 min), respectively. No obvious body

weight loss was observed for all groups during the CPPT process in a week. Then they were all sacrificed to collect the peripheral blood mononuclear cells (PBMC) and bone marrow (BM) to analyze the expression of AML stem cell marker CD34. The immunohistochemical analysis of bone marrow (BM) was further conducted. The results showed that CD34 expressed in **H4–PEG-Glu** under the 808 nm laser irradiation group (the right images in Fig. 6d) was obviously lower than that in the control group (left images in Fig. 6d) and in the **H4–PEG-Glu** group (the middle images in Fig. 6d). The CD34$^+$ cells in all three groups were also quantified by flow cytometry. The percentage of CD34$^+$ cells in PBMC and bone marrow with **H4–PEG-Glu** under 808 nm laser irradiation was significantly lower than that of the other two groups (Fig. 6c). To assess the hepatotoxicity of **H4–PEG-Glu**, **H4–PEG-Glu** (200 µg) and PBS were injected in ICR female mice ($n = 3$ per group, ~20 g each), respectively. The blood was collected at 7 days post-injection to analyze the biochemistry index (ALT, AST, CREA, BUN). The concentration in the experiment group was similar to that in the PBS group, indicating that **H4–PEG-Glu** has no obvious toxicity to the kidneys and liver (Fig. S11†). All the above results demonstrated that **H4–PEG-Glu** is a potential small-molecule NIR-II probe for clinical translation in AML cancer theranostics.

Experimental section

Methods and materials are provided in the ESI. All animal experiments were approved by the Chinese Regulations for the Administration of Affairs Concerning Experimental Animals and Institutional Animal Care and Use Committee (IACUC) of Wuhan University. The study has been approved by the Institutional Ethical Committee of Zhongnan Hospital of Wuhan University, China (No. 2018278), and performed in accordance with the ethical standards as laid down in the 1964 Helsinki declaration and its later amendments or comparable ethical standards.

Conclusions

In conclusion, we have successfully designed and synthesized a novel mitochondria-targeted NIR-II fluorophore **H4–PEG-Glu** with a new thiopyrylium skeleton for AML CPTT. **H4–PEG-Glu** showed excellent water solubility, high photo-stability and biocompatibility, and superior targeting affinity toward AML cancer cells (THP-1 and Molm-13) and peripheral blood donated from AML patients. **H4–PEG-Glu** not only can quickly and effectively image mitochondria in acute myeloid leukemia (AML) cells, and induce G_0/G_1 phase arrest by the intrinsic mitochondrial apoptosis pathway w/o irradiation, but also exhibited moderate cytotoxicity against AML cancer cells in a dose dependent-manner without laser irradiation. THP-1 and Molm-13 cells treated with **H4–PEG-Glu** upon NIR laser irradiation showed enhanced CPTT with 93.07% ± 6.43 and 89.44% ± 2.84 apoptosis by Annexin V staining. AML patient derived PDX mouse models were finally used for the first time for *in vivo* mitochondria-targeted NIR-II Imaging of acute myeloid leukemia and image-guided CPTT. The percentage of CD34$^+$

cells in PBMC and bone marrow was significantly reduced after **H4–PEG-Glu** treatment and laser irradiation. To the best of our knowledge, this is the first NIR-II small-molecule probe for mitochondrial-targeted chemo- and photothermal synergistic therapy for AML cancer. It is hoped that this novel NIR-II cation fluorophore may provide a practical strategy to develop small-molecule NIR-II fluorophores for non-solid tumor therapy with a deeper penetration depth and higher resolution.

Conflicts of interest

There are no conflicts to declare.

Acknowledgements

Notes and references

1 (a) D. Jaque, L. Martínez Maestro, B. Del Rosal, P. Haro-Gonzalez, A. Benayas, J. L. Plaza, E. Martín Rodríguez and J. García Solé, *Nanoscale*, 2014, **6**, 9494–9530; (b) H. He, J. Wang, H. Wang, N. Zhou, D. Yang, D. R. Green and B. Xu, *J. Am. Chem. Soc.*, 2018, **140**, 1215–1218; (c) Y. Liu, J. Zhou, L. Wang, X. Hu, X. Liu, M. Liu, Z. Cao, D. Shangguan and W. Tan, *J. Am. Chem. Soc.*, 2016, **138**, 12368–12374; (d) R. M. Shallis, R. Wang, A. Davidoff, X. Ma and A. M. Zeidan, *Blood Rev.*, 2019, **36**, 70–87.

2 H. S. Jung, J.-H. Lee, K. Kim, S. Koo, P. Verwilst, J. L. Sessler, C. Kang and J. S. Kim, *J. Am. Chem. Soc.*, 2017, **139**, 9972–9978.

3 (a) R. Guo, J. Yin, Y. Ma, Q. Wang and W. Lin, *J. Mater. Chem. B*, 2018, **6**, 2894–2900; (b) Y. Koide, Y. Urano, S. Kenmoku, H. Kojima and T. Nagano, *J. Am. Chem. Soc.*, 2007, **129**, 10324–10325; (c) M. Sibrian-Vazquez, I. V. Nesterova, T. J. Jensen and M. G. H. Vicente, *Bioconjugate Chem.*, 2008, **19**, 705–713; (d) J. Zielonka, J. Joseph, A. Sikora, M. Hardy, O. Ouari, J. Vasquez-Vivar, G. Cheng, M. Lopez and B. Kalyanaraman, *Chem. Rev.*, 2017, **117**, 10043–10120.

4 (a) G. Cheng, J. Zielonka, B. P. Dranka, D. McAllister, A. C. Mackinnon, J. Joseph and B. Kalyanaraman, *Cancer Res.*, 2012, **72**, 2634–2644; (b) J. C. Wang, Z. Jiang, L. P. Xiang, Y. F. Li, M. R. Ou, X. Yang, J. W. Shao, Y. S. Lu, L. F. Lin, J. Z. Chen, Y. Dai and L. Jia, *Sci. Rep.*, 2014, **4**, 5006; (c) B. Kalyanaraman, G. Cheng, M. Hardy, O. Ouari,

M. Lopez, J. Joseph, J. Zielonka and M. B. Dwinell, *Redox Biol.*, 2018, **14**, 316–327.

5 H. Chen, J. Wang, X. Feng, M. Zhu, S. Hoffmann, A. Hsu, K. Qian, D. Huang, F. Zhao, W. Liu, H. Zhang and Z. Cheng, *Chem. Sci.*, 2019, **10**, 7946–7951.

6 (*a*) H. Dohner, D. J. Weisdorf and C. D. Bloomfield, *N. Engl. J. Med.*, 2015, **373**, 1136–1152; (*b*) J. N. Saultz and R. Garzon, *J. Clin. Med.*, 2016, **5**, 33; (*c*) B. M. Barth, E. I. Altinoğlu, S. S. Shanmugavelandy, J. M. Kaiser, D. Crespo-Gonzalez, N. A. Divittore, C. Mcgovern, T. M. Goff, N. R. Keasey, J. H. Adair, T. P. Loughran, D. F. Claxton and M. Kester, *ACS Nano*, 2011, **5**, 5325–5337.

7 (*a*) P. Bose, P. Vachhani and J. E. Cortes, *Curr. Treat. Options Oncol.*, 2017, **18**, 17; (*b*) K. D. Miller, L. Nogueira, A. B. Mariotto, J. H. Rowland, K. R. Yabroff, C. M. Alfano, A. Jemal, J. L. Kramer and R. L. Siegel, *Ca-Cancer J. Clin.*, 2019, **69**, 363–385.

8 (*a*) W. Wang, G. Liang, W. Zhang, D. Xing and X. Hu, *Chem. Mater.*, 2018, **30**, 3486–3498; (*b*) Y. Chen, Z. Li, H. Wang, Y. Wang, H. Han, Q. Jin and J. Ji, *ACS Appl. Mater. Interfaces*, 2016, **8**, 6852–6858; (*c*) Y. Zhang, C. Y. Ang, M. Li, S. Y. Tan, Q. Qu and Y. Zhao, *ACS Appl. Mater. Interfaces*, 2016, **8**, 6869–6879.

9 (*a*) S. Kunjachan, J. Ehling, G. Storm, F. Kiessling and T. Lammers, *Chem. Rev.*, 2015, **115**, 10907–10937; (*b*) G. Hong, J. C. Lee, J. T. Robinson, U. Raaz, L. Xie, N. F. Huang, J. P. Cooke and H. Dai, *Nat. Med.*, 2012, **18**, 1841–1846; (*c*) G. Hong, S. Diao, J. Chang, A. L. Antaris, C. Chen, B. Zhang, S. Zhao, D. N. Atochin, P. L. Huang, K. I. Andreasson, C. J. Kuo and H. Dai, *Nat. Photonics*, 2014, **8**, 723; (*d*) B. Li, L. Lu, M. Zhao, Z. Lei and F. Zhang, *Angew. Chem., Int. Ed.*, 2018, **57**, 7483; (*e*) C. Qu, Y. Xiao, H. Zhou, B. Ding, A. Li, J. Lin, X. Zeng, H. Chen, K. Qian, X. Zhang, W. Fang, J. Wu, Z. Deng, Z. Cheng and X. Hong, *Adv. Opt. Mater.*, 2019, **7**, 1900229.

10 (*a*) D. Kim, N. Lee, Y. I. Park and T. Hyeon, *Bioconjugate Chem.*, 2017, **28**, 115–123; (*b*) G. Hong, S. Diao, A. L. Antaris and H. Dai, *Chem. Rev.*, 2015, **115**, 10816–10906; (*c*) H. Zhang, Z.-H. Chen, X. Liu and F. Zhang, *Nano Res.*, 2020, **13**, 1795–1809.

11 (*a*) K. Li and B. Liu, *Chem. Soc. Rev.*, 2014, **43**, 6570–6597; (*b*) Y. Liu, J. Liu, D. Chen, X. Wang, Z. Liu, H. Liu, L. Jiang, C. Wu and Y. Zou, *Macromolecules*, 2019, **52**, 5735–5740; (*c*) B. Guo, J. Chen, N. Chen, M. Wu, K. Li, C. Liu and B. Liu, *Adv. Mater.*, 2019, **31**, 1808355; (*d*) Z. Zhang, X. Fang, Z. Liu, H. Liu, D. Chen, S. He, X. Zhang and C. Wu, *Angew. Chem., Int. Ed.*, 2020, **59**, 3691–3698; (*e*) H. Zhou, S. Li, X. Zeng, M. Zhang, L. Tang, Q. Li, D. Chen, X. Meng and X. Hong, *Chin. Chem. Lett.*, 2020, **31**, 1382–1386.

12 (*a*) S. He, J. Song, J. Qu and Z. Cheng, *Chem. Soc. Rev.*, 2018, **47**, 4258–4278; (*b*) J. Li, Y. Liu, Y. Xu, L. Li, Y. Sun and W. Huang, *Coord. Chem. Rev.*, 2020, **415**, 213318; (*c*) B. Li, M. Zhao and F. Zhang, *ACS Mater. Lett.*, 2020, **2**, 905–917; (*d*) C. Sun, B. Li, M. Zhao, S. Wang, Z. Lei, L. Lu, H. Zhang, L. Feng, C. Dou, D. Yin, H. Xu, Y. Cheng and F. Zhang, *J. Am. Chem. Soc.*, 2019, **141**, 19221–19225; (*e*) Q. Wang, Y. Dai, J. Xu, J. Cai, X. Niu, L. Zhang, R. Chen, Q. Shen, W. Huang and Q. Fan, *Adv. Funct. Mater.*, 2019, **29**, 1901480.

13 (*a*) Y. Du, B. Xu, T. Fu, M. Cai, F. Li, Y. Zhang and Q. Wang, *J. Am. Chem. Soc.*, 2010, **132**, 1470–1471; (*b*) J. Lin, Q. Li, X. Hong and Y. Xiao, *Sci. China: Chem.*, 2020, **63**, 766–770; (*c*) C. Li, Y. Zhang, M. Wang, Y. Zhang, G. Chen, L. Li, D. Wu and Q. Wang, *Biomaterials*, 2014, **35**, 393–400; (*d*) C. Li, W. Li, H. Liu, Y. Zhang, G. Chen, Z. Li and Q. Wang, *Angew. Chem., Int. Ed.*, 2020, **132**, 253–258; (*e*) M. Zhang, J. Yue, R. Cui, Z. Ma, H. Wan, Y. Zhou, Y. Kuang, Y. Zhong, D. W. Pang and H. Dai, *Proc. Natl. Acad. Sci. U. S. A.*, 2018, **115**, 6590.

14 H. Liu, G. Hong, Z. Luo, J. Chen, J. Chang, M. Gong, H. He, J. Yang, X. Yuan, L. Li, X. Mu, J. Wang, W. Mi, J. Luo, J. Xie and X.-D. Zhang, *Adv. Mater.*, 2019, **31**, 1901015.

15 (*a*) K. Welsher, Z. Liu, S. P. Sherlock, J. T. Robinson, Z. Chen, D. Daranciang and H. Dai, *Nat. Nanotechnol.*, 2009, **4**, 773–780; (*b*) S. Diao, G. Hong, J. T. Robinson, L. Jiao, A. L. Antaris, J. Z. Wu, C. L. Choi and H. Dai, *J. Am. Chem. Soc.*, 2012, **134**, 16971; (*c*) C. Liang, S. Diao, C. Wang, H. Gong, T. Liu, G. Hong, X. Shi, H. Dai and Z. Liu, *Adv. Mater.*, 2014, **26**, 5646; (*d*) J. D. Harvey, P. V. Jena, H. A. Baker, G. H. Zerze, R. M. Williams, T. V. Galassi, D. Roxbury, J. Mittal and D. A. Heller, *Nat. Biomed. Eng.*, 2017, **1**, 0041.

16 (*a*) Y. Zhong, Z. Ma, S. Zhu, J. Yue, M. Zhang, A. L. Antaris, J. Yuan, R. Cui, H. Wan, Y. Zhou, W. Wang, N. F. Huang, J. Luo, Z. Hu and H. Dai, *Nat. Commun.*, 2017, **8**, 737; (*b*) P. Wang, Y. Fan, L. Lu, L. Liu, L. Fan, M. Zhao, Y. Xie, C. Xu and F. Zhang, *Nat. Commun.*, 2018, **9**, 2898; (*c*) Y. Fan and F. Zhang, *Adv. Opt. Mater.*, 2019, **7**, 1801417; (*d*) H. Zhou, Y. Xiao and X. Hong, *Chin. Chem. Lett.*, 2018, **29**, 1425–1428.

17 (*a*) A. L. Antaris, H. Chen, K. Cheng, Y. Sun, G. Hong, C. Qu, S. Diao, Z. Deng, X. Hu, B. Zhang, X. Zhang, O. K. Yaghi, Z. R. Alamparambil, X. Hong, Z. Cheng and H. Dai, *Nat. Mater.*, 2016, **15**, 235–242; (*b*) A. L. Antaris, H. Chen, S. Diao, Z. Ma, Z. Zhang, S. Zhu, J. Wang, A. X. Lozano, Q. Fan, L. Chew, M. Zhu, K. Cheng, X. Hong, H. Dai and Z. Cheng, *Nat. Commun.*, 2017, **8**, 15269; (*c*) H. Zhou, X. Zeng, A. Li, W. Zhou, L. Tang, W. Hu, Q. Fan, X. Meng, H. Deng, L. Duan, Y. Li, Z. Deng, X. Hong and Y. Xiao, *Nat. Commun.*, 2020, **11**, 6183.

18 (*a*) B. Li, Z. Lei and F. Zhang, *Angew. Chem., Int. Ed.*, 2018, **57**, 7483–7487; (*b*) J. Yang and X. Hong, *Sci. China: Chem.*, 2019, **62**, 7–8.

19 Q. Li, Q. Ding, Y. Li, X. Zeng, Y. Liu, S. Lu, H. Zhou, X. Wang, J. Wu, X. Meng, Z. Deng and Y. Xiao, *Chem. Commun.*, 2020, **56**, 3289.

20 Y. Li, Y. Liu, Q. Li, X. Zeng, T. Tian, W. Zhou, Y. Cui, X. Wang, X. Cheng, Q. Ding, X. Wang, J. Wu, H. Deng, Y. Li, X. Meng, Z. Deng, X. Hong and Y. Xiao, *Chem. Sci.*, 2020, **11**, 2621–2626.

21 Y. Li, Z. Cai, S. Liu, H. Zhang, S. T. H. Wong, J. W. Y. Lam, R. T. K. Kwok, J. Qian and B. Z. Tang, *Nat. Commun.*, 2020, **11**, 1255.

22 L. Szablewski, *Biochim. Biophys. Acta*, 2013, **1835**, 164–169.

23 (*a*) H. Zhang, Y. Fan, P. Pei, C. Sun, L. Lu and F. Zhang, *Angew. Chem., Int. Ed.*, 2019, **58**, 10153–10157; (*b*) B. Li, M. Zhao, L. Feng, C. Dou, S. Ding, G. Zhou, L. Lu, H. Zhang, F. Chen, X. Li, G. Li, S. Zhao, C. Jiang, Y. Wang, D. Zhao, Y. Cheng and F. Zhang, *Nat. Commun.*, 2020, **11**, 3102; (*c*) H. Ma, C. Liu, Z. Hu, P. Yu, X. Zhu, R. Ma, Z. Sun, C.-H. Zhang, H. Sun, S. Zhu and Y. Liang, *Chem. Mater.*, 2020, **32**, 2061–2069; (*d*) Q. Yang, Z. Hu, S. Zhu, R. Ma, H. Ma, Z. Ma, H. Wan, T. Zhu, Z. Jiang, W. Liu, L. Jiao, H. Sun, Y. Liang and H. Dai, *J. Am. Chem. Soc.*, 2018, **140**, 1715–1724.

24 (*a*) Y.-X. Zhu, H.-R. Jia, G. Gao, G.-Y. Pan, Y.-W. Jiang, P. Li, N. Li, C. Zhou, C. She, N. W. Ulrich, Z. Chen and F.-G. Wu, *Biomaterials*, 2020, **232**, 119668; (*b*) G.-Y. Pan, H.-R. Jia,

Y.-X. Zhu, R.-H. Wang, F.-G. Wu and Z. Chen, *ACS Biomater. Sci. Eng.*, 2017, **3**, 3596–3606.

25 (*a*) B. Ding, Y. Xiao, H. Zhou, X. Zhang, C. Qu, F. Xu, Z. Deng, Z. Cheng and X. Hong, *J. Med. Chem.*, 2019, **62**, 2049–2059; (*b*) X. Hong, H. Zhou, Y. Xiao, B. Ding, J. Duan, CN Pat., 109369633B, 2018.

26 X. Yang, D. Wang, Y. Shi, J. Zou, Q. Zhao, Q. Zhang, W. Huang, J. Shao, X. Xie and X. Dong, *ACS Appl. Mater. Interfaces*, 2018, **10**, 12431–12440.

27 X.-S. Hou, H.-S. Wang, B. P. Mugaka, G.-J. Yang and Y. Ding, *Biomater. Sci.*, 2018, **6**, 2786–2797.

28 X. Li, M. Tian, G. Zhang, R. Zhang, R. Feng, L. Guo, X. Yu, N. Zhao and X. He, *Anal. Chem.*, 2017, **89**, 3335–3344.